sustainability

MDPI

Article

Infrared Precursor Experiment to Predict Water Inrushes in Underground Spaces Using a Multiparameter Normalization

Kewang Cao [1,2], Furong Dong [1,2], Liqiang Ma [2,*], Naseer Muhammad Khan [3,*], Tariq Feroze [3], Saad S. Alarifi [4], Sajjad Hussain [5] and Muhammad Ali [6]

[1] School of Art, Anhui University of Finance and Economics, Bengbu 233030, China
[2] School of Mines, China University of Mining and Technology, Xuzhou 221116, China
[3] Department of Sustainable Advanced Geomechanical Engineering, Military College of Engineering, National University of Sciences and Technology, Risalpur 23200, Pakistan
[4] Department of Geology and Geophysics, College of Science, King Saud University, P.O. Box 2455, Riyadh 11451, Saudi Arabia
[5] Department of Mining Engineering, University of Engineering & Technology, Peshawar 25000, Pakistan
[6] Australia Education Management Group, 635 Canterbury Road, Surrey Hills, VIC 3127, Australia
* Correspondence: ckma@cumt.edu.cn (L.M.); nmkhan@mce.edu.pk (N.M.K.)

Abstract: Rock failure is the root cause of geological disasters such as slope failure, civil tunnel collapse, and water inrush in roadways and mines. Accurate and effective monitoring of the loaded rock failure process can provide reliable precursor information for water inrushes in underground engineering structures such as in mines, civil tunnels, and subways. The water inrush may affect the safe and efficient execution of these engineering structures. Therefore, it is essential to predict the water inrush effectively. In this paper, the water inrush process of the roadway was simulated by laboratory experiments. The multiparameters such as strain energy field and infrared radiation temperature field were normalized based on the normalization algorithm of linear function transformation. On the basis of analyzing the variation characteristics of the original parameters, the evolution characteristics after the parameters normalization algorithm were studied, and the precursor of roadway water inrush was predicted comprehensively. The results show that the dissipation energy ratio, the infrared radiation variation coefficient (IRVC), the average infrared radiation temperature (AIRT), and the variance of successful minor infrared image temperature (VSMIT) are all suitable for the prediction of roadway water inrushes in the developing face of an excavation. The intermediate mutation of the IRVC can be used as an early precursor of roadway water inrush in the face of an excavation that is being developed. The inflection of the dissipation energy ratio from a declining amount to a level value and the mutation of VSMIT during rock failure can be used as the middle precursor of roadway water inrush. The mutation of AIRT and VSMIT after rock failure can be used as the precursor of roadway imminent water inrush. Combining with the early precursor and middle precursor of roadway water inrush, the graded warning of "early precursor–middle precursor–final precursor" of roadway water inrush can be obtained. The research results provide a theoretical basis for water inrush monitoring and early warning in the sustainable development of mine, tunnel, shaft, and foundation pit excavations.

Keywords: water inrush; precursor; strain energy; infrared radiation; normalized; sustainable mine

Citation: Cao, K.; Dong, F.; Ma, L.; Khan, N.M.; Feroze, T.; S. Alarifi, S.; Hussain, S.; Ali, M. Infrared Precursor Experiment to Predict Water Inrushes in Underground Spaces Using a Multiparameter Normalization. *Sustainability* **2023**, *15*, 7570. https://doi.org/10.3390/su15097570

Academic Editor: Jianjun Ma

Received: 16 February 2023
Revised: 26 April 2023
Accepted: 1 May 2023
Published: 5 May 2023

1. Introduction

Due to the rapid development of underground spaces such as subways, tunnels, and caverns, large-scale geological disasters such as water inrushes, mud rushes, and rock collapses often occur in the construction stage [1–7]. In coal mining, water inrush accidents often occur, resulting in serious and often irreparable property losses and casualties, seriously affecting the normal production of coal mines [8,9]. It is therefore important to carry out relevant underground development face water inrush laboratory experiments to determine the variation characteristics of water inrush precursor information; this can not only improve the reliability of water inrush prediction in underground space development but also meet the needs of sustainable protection of mining water resources. Water resource protection is the theme of sustainable development of mining ecological environments and a key way to achieve green mining.

Mining and underground civil activities inevitably lead to the redistribution of underground rock stress and fracture damage of rock, which greatly change the permeability of surrounding rock. This can lead to water inrush mainly in the roof, through stress-induced natural fractures or geology features, causing safety accidents.

In subway construction, damage to the lining of shield tunnels may cause water inrush in the subway. This is caused by nonwatertight drilling of through-holes near the intersection of two subway tunnels. Under high hydraulic gradients, weak permeable areas form and extend, leading to soil water slurry explosions [10–13]. The infrared radiation information of rock changes during the process of stress redistribution and consequent fracture damage process [14–20]. Monitoring the infrared radiation released to the outside during the process of rock loading can predict the characteristics and process of rock deformation and failure. This provides reliable information for the establishment of rock failure precursors [21–29]. In recent years, many scholars have carried out considerable research using the infrared radiation characteristics of rock fracture and water seepage. Asakura et al. [30] studied the infrared radiation monitoring of water leakage in tunnel lining and proved the feasibility of monitoring water leakage by infrared technology. Liu et al. [31] studied the characteristics of infrared radiation in the process of concrete fracture and water seepage and found that the "initial increase followed by a decrease" in the curve of infrared radiation temperature was an abnormal precursor of the infrared radiation of concrete fracture and water seepage. Dou et al. [32] carried out the infrared radiation observation experiments of tunnel leakage, studied the infrared radiation variation characteristics, and wrote the MATLAB image processing program to extract the infrared image characteristics during the process of concrete leakage. Zhang [33] studied the characteristics of infrared radiation in the process of sandstone fracture and water inrush, in which the sudden decrease of infrared radiation temperature predicted the occurrence of roadway water inrush, and the accelerated rate of infrared radiation temperature could be used as a precursor for water inrushes.

To quantitatively analyze the characteristics of infrared radiation in the process of rock fracture and water seepage, Wu et al. [34] first proposed the average infrared radiation temperature (AIRT) index of rock surface. Liu [35] used the AIRT index to analyze the infrared radiation characteristics of dry and water saturated rocks during uniaxial loading, and found that water can promote the AIRT of a rock surface. However, different areas of the rock surface may simultaneously heat up and cool down during the unstable development crack development stage in the rock, resulting in no change in overall AITR index [36]. Therefore, Liu [37], Ma et al. [38], and Yang [39] proposed the infrared radiation variance (*IRV*), variance of successful minor infrared image temperature (*VSMIT*), and infrared radiation variation coefficient (*IRCV*) of rock surface. The results show that the above indexes can well reflect the differentiation characteristics of infrared radiation on the rock surface. For example, Ma and Zhang [38] studied the internal relationship between stress adjustment (due to excavating) and *VSMIT* index during the loading process of dry and water-saturated rocks, and found that *VSMIT* index can correlate well with the rock failure and water has an amplification effect on the mutation characteristics of *VSMIT* index.

Although scholars have carried out a lot of research work on the monitoring and warning of water inrush during underground development, the results to date have not proved reliable for detecting an imminent water inrush. This is mainly due to the localized complex geology and hydrology. Based on the analysis of the physical parameters such as stress, infrared radiation, and strain energy in the process of predicting roadway water inrushes, this paper normalizes each physical parameter, then comprehensively analyzes the multielement information evolution characteristics and their correlation with roadway water inrushes, and studies the comprehensive precursor characteristics of them. This study proposes an early warning precursor and monitoring the occurrence of roadway water inrush. The research findings will provide a theoretical basis for monitoring and early warning of water inrush in underground spaces for their safe and efficient development.

2. Experimental Principle

Stefan–Boltzmann's law states that any object above absolute zero will radiate electromagnetic waves to the outside world. Due to this, the radiation intensity and the temperature of the object satisfy the following formula [39]:

$$J^* = \varepsilon\sigma T^4 \tag{1}$$

where J^* represents the total energy radiated by the object per unit area, $W \cdot m^{-2}$; ε represents the surface emissivity of the object, $0 < \varepsilon < 1$; σ is the Stefan–Boltzmann constant, $5.670373 \times 10^{-8}\ W \cdot m^{-2} \cdot K^{-4}$; T is the absolute temperature of the surface, K.

This law explains how the infrared radiation on the surface of the object at room temperature is affected. Further, the relationship between the radiation intensity and the temperature of the object satisfies the fourth power. The force exerted on a solid causes changes in the distance between internal particles, resulting in thermodynamic changes and, thus, temperature changes. This phenomenon of temperature change caused by heat generated due to force can be referred to as the thermal–mechanical coupling effect [36]. Materials with different mechanical properties (such as elastic materials, elastoplastic materials, viscoelastic materials, etc.) and the same material have different thermal and mechanical coupling effects at different stress stages. These different thermodynamic coupling effects have different characteristics and laws due to their different microscopic mechanisms. In the elastic range, the object undergoes the process of tension or compression accompanied by the reversible conversion of heat. In the adiabatic environment, the sum of temperature and principal stress satisfies the linear relationship [40]:

$$\Delta T = \frac{\alpha}{\rho C_\sigma} T S \tag{2}$$

where ΔT and T are the change of object temperature and object temperature, respectively; α is the linear coefficient of thermal expansion; C_σ is the specific heat coefficient under constant stress; S is the sum of the principal stresses.

The change of principal stress during uniaxial rock loading is only related to σ_1. The fourth term represents the internal dissipated energy of the material, which is manifested in the thermoelastoplastic comprehensive effect at this stage. The work carried out by the external force is not all transformed into the internal thermal energy of the material but is mostly consumed in the process of internal microstructure change. Plastic deformation in the process of energy dissipation and thermal energy conversion is not reversible, and ΔE mainly includes the following three parts in the process of energy consumption [36]:

$$\Delta E = \Delta E_1 + \Delta E_2 + \Delta E_3 \tag{3}$$

ΔE_1 is the energy carried by the escape process of pore gas, in general, $\Delta E_1 < 0$. ΔE_2 is the energy consumed by the expansion of pores, fractures, and joints and the generation of new fractures in the rock. The internal pores, fractures, and joint weak surfaces will first contract and close with the increase of stress. The pores will then collapse, and the primary fractures and joints will further expand, penetrate, and merge. Moreover, the new fractures will be generated by the increase in stress. The ΔE_2 is less than 0 due to the consumption of energy in this process. ΔE_3 is the energy generated by friction because there are friction behaviors among the pores, fissures, joints, and rock particles along all directions in the interior of the rock. Two factors influence the process of frictional heat generation: one is the positive pressure on the contact surface inside the rock, and the other is the friction coefficient. When the friction coefficient is fixed, the friction force is positively related to the normal stress on the contact surface. The larger the friction force, the more work will be carried out to overcome the friction force in the process of crack and particle sliding, resulting in the higher energy consumption. It is important to note that in this process the temperature of the contact surface due to friction heat production will increase, therefore ΔE_3 is greater than zero.

3. Experimental Design

3.1. Experimental Equipment

The experimental loading equipment used an SANS electronic universal testing machine system with a maximum vertical load of 1000 kN. The water pressure loading equipment adopts a Shanghai SB water pressure pump, the maximum working pressure is 10 MPa, and the water pressure is set to 0.5 MPa. The infrared radiation detection device adopts the American FLIRA615 infrared thermal imager, whose thermal sensitivity is 0.025 °C, and the wavelength range is 7.5–14.0 m. The image acquisition rate was set at 25 frames/s.

3.2. Rock Samples

The representative samples of sandstone collected from a coal mine in Shandong province were used in the laboratory experimental process. All samples were obtained from the same rock sample. The specimen design specification is a cuboid of 100 × 100 × 150 mm. The diameter and depth of the observation hole in the test block are 50 mm, and the diameter and depth of the water injection hole are 50 mm and 50 mm. A total of five specimens were prepared, represented by A1, A2, A3, A4, and A5. The actual measurement specifications of these specimens are shown in Table 1. The rock sample model is shown in Figure 1a, and the processed specimen is shown in Figure 1b. The water gushing from the tunnel mainly comes from the rich water in front of the tunnel face, so this special test piece shape is designed. The first section of the water injection hole of the rock sample is bonded together with the iron block of the fixed abrasive tool using strong adhesive, and then the fixed abrasive tool is reinforced by electric welding to resist the water pressure in the water injection hole after the water pump is running. The water injection pipe and the abrasive tool are tightened and fixed by screws to ensure that there is no water leakage on the water injection side during the experiment. The following figure shows the fixed mold of the rock sample.

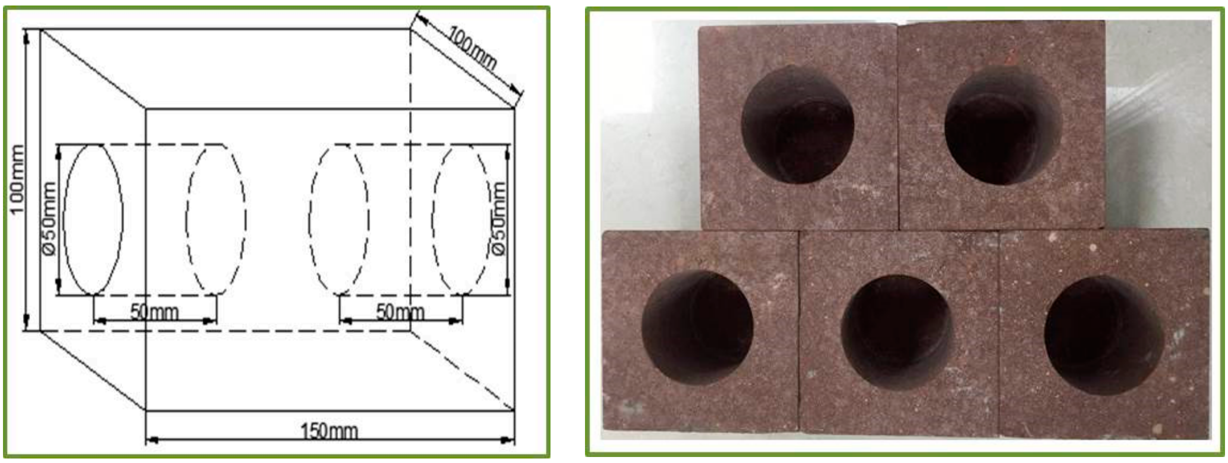

(**a**) rock sample structure (**b**) rock sample picture

Figure 1. Schematic diagram of rock sample.

Table 1. Actual measurement specifications of the specimen.

Number	Length × Width × Height (mm)	Observation Hole Diameter × Depth (mm)	Water Injection Hole Diameter × Depth (mm)
A_1	150.32 × 100.42 × 99.85	φ50.24 × 50.53	φ50.23 × 50.66
A_2	150.31 × 100.48 × 100.38	φ50.22 × 50.68	φ50.23 × 50.97
A_3	150.10 × 100.12 × 99.78	φ50.22 × 50.34	φ50.25 × 50.35
A_4	149.97 × 100.10 × 99.25	φ50.25 × 50.58	φ50.24 × 50.59
A_5	150.35 × 100.31 × 99.77	φ50.23 × 50.73	φ50.22 × 50.67

3.3. Experiment Process

The rock specimen was loaded uniaxially with a closure rate of 0.1 mm/min. The data acquisition frequency of the testing machine was set as 10 times/s. The layout of the experimental equipment is shown in Figure 2. To facilitate the sorting and analysis of test data, the water pressure of the water pump was set as 0.5 MPa before the test, and the thermal imager was installed about 1 m away from the sample to observe the infrared temperature field changes on the sample surface. The experiment was started after the infrared radiation temperature on the rock surface remained stable. We synchronously calibrated the time of all test equipment. In addition, the start and end times of each equipment remained the same. Then, uniaxial loading was applied to the rock sample until inrush water appeared.

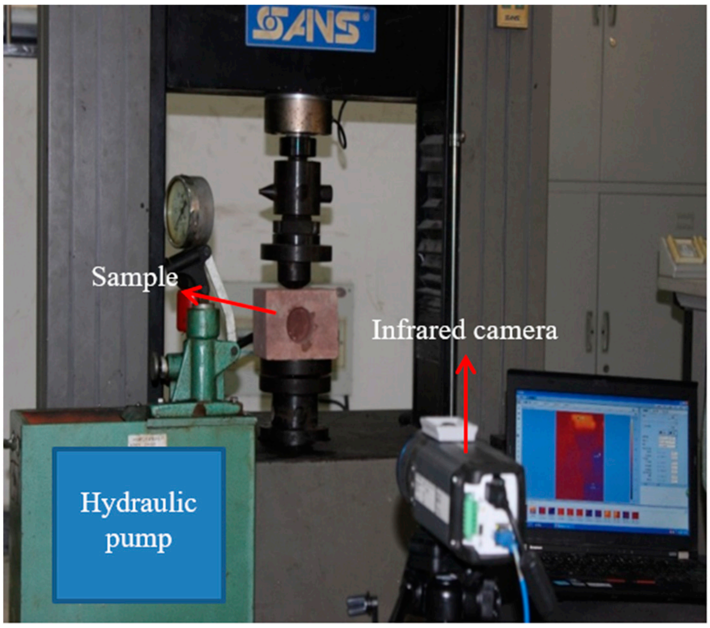

Figure 2. Experimental layout.

4. Indicators

4.1. Strain Energy

Assuming that a rock unit deforms under the action of external forces and the process occurs in a closed system, according to the first law of thermodynamics, the following can be obtained:

$$U = U^d + U^e \tag{4}$$

where U is the total strain energy, which is determined by the stress–strain curve and the area around the horizontal axis, U^d is the dissipated strain energy of the unit, and U^e is the elastic strain energy released by the unit.

Figure 3 shows the relationship between U^d and U^e during uniaxial rock loading. The releasable elastic strain energy U^e in the uniaxial loading process of rock can be rewritten as follows [41,42]:

$$U^e = \frac{1}{2E_u}\sigma^2 \tag{5}$$

where E_u is the unloading modulus of elasticity.

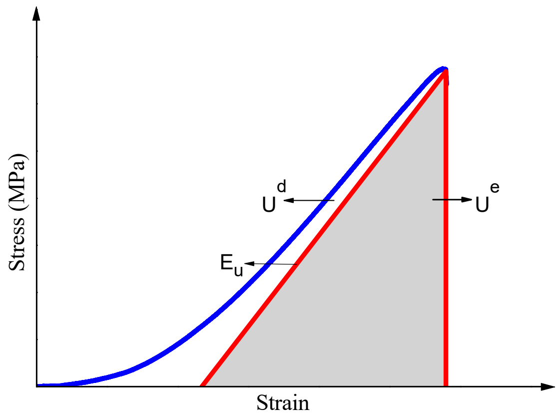

Figure 3. Relationship between dissipated strain energy and elastic strain energy in the stress–strain curve.

In order to facilitate calculation, the elastic modulus E_0 is generally used instead of E_u. In this paper, the average modulus is used to calculate the elastic modulus, and the stress–strain formula is assumed to be σ = f (ε). The following formula obtains the elastic modulus

$$E = \frac{f(\varepsilon_2) - f(\varepsilon_1)}{\varepsilon_2 - \varepsilon_1} \tag{6}$$

where E is the elastic modulus, and f (ε_1) and f (ε_2) are the stress values corresponding to the starting and ending points of the elastic phase, respectively.

4.2. Infrared Thermal Image

Infrared thermal image is a series of object surface temperature distribution images output by an infrared thermal imager. The two-dimensional temperature matrix of frame p in the original infrared thermal image is [43]:

$$f_p(x,y) \tag{7}$$

where p is the frame number index of the infrared thermal image sequence; x and y represent the row and column numbers of the thermal imager temperature matrix, respectively.

4.3. VSMIT

VSMIT can reflect the dispersion degree of infrared radiation temperature value of the entire rock sample surface, which is defined as follows [43]:

$$VSMIT = \frac{1}{M}\frac{1}{N}\sum_{y=1}^{N}\sum_{x=1}^{M}[f_p(x,y) - AIRT_p]^2 \tag{8}$$

Among them, $AIRT_p = \frac{1}{M}\frac{1}{N}\sum\limits_{y=1}^{N}\sum\limits_{x=1}^{M} f_p(x,y)$; M and N are the maximum numbers of rows and columns for x and y, respectively.

4.4. IRVC

The *IRVC* can measure the dispersion degree of the infrared radiation temperature field on the rock surface, which is defined as follows [39]:

$$IRVC = \sigma / AIRT \tag{9}$$

where σ is the standard deviation of infrared radiation temperature on the rock surface.

5. Experimental Results

5.1. Strain Energy

The deformation and failure of rock is a process of energy input, elastic energy accumulation, energy dissipation, and energy release from the point of view of strain energy. Energy dissipation is mainly used for crack initiation and propagation, and energy release is the internal cause of the sudden failure of the rock mass. The elastic strain energy accumulated by the rock mass before excavation is the main source of the energy released by the ultimate failure of the surrounding rock mass, especially the deep hard brittle rock mass with good energy storage under the condition of high in situ stress. A large amount of elastic strain energy accumulated in the excavation is released instantly due to the excavation unloading effect, promoting the occurrence of rock mass failure and then connecting the water diversion fissure channel, finally resulting in a water inrush accident.

Figure 4 shows the strain energy evolution curve during the loading process of the rock sample. Due to space limitations, samples A_1, A_2, and A_3 were selected for analysis in this paper. As shown in Figure 4, the energy absorbed in the rock at the beginning of loading is mainly dissipated strain energy, because most of the strain energy is consumed by pore and microfracture compaction. The curves of elastic strain energy and dissipated strain energy diverge with the increase of stress, and the growth of elastic strain energy increases continuously, while the dissipated strain energy increases in a nearly straight line, which is used for the formation and expansion of plastic deformation and microcracks in rocks. The elastic strain energy drops sharply, while the dissipated strain energy increases sharply at the peak stress, which indicates that the internal microcrack propagation and penetration rate accelerated and the damage was aggravated. After the peak stress, the bearing capacity of the rock decreases rapidly and maintains a certain residual strength. The strain energy absorbed by the rock is transformed into dissipative strain energy in this period, which is used for the further development of rock fracture and shear deformation along the slip surface. Then, a macroscopic water diversion channel is formed in the rock, and water inrush eventually occurs in the roadway.

The dissipated strain energy ratio of rock refers to the proportion of dissipated strain energy to the total strain energy. The dissipated strain energy ratio curve shows a trend of decline before the peak stress, changes from a decline to a level near the peak stress when approaching the peak stress, and then begins to increase. The curve changes abruptly with the rock failure. After that, the dissipated strain energy ratio curve continues to increase until a water inrush occurs in the rock face. The analysis found that the strain energy dissipation ratio curve of samples experienced a "decline-level" process when the rock approached failure. This is due to the dissipated strain energy used for plastic strain and crack growth increasing with the rapid development of microcracks in the rock; although the elastic strain energy is still accumulating, the rock will reach the maximum energy storage limit. Therefore, the dissipated strain energy ratio of rock declines to the level, and then the elastic strain energy reaches the energy storage limit. The accumulated elastic strain energy is quickly released and causes rock failure. In summary, the turning point of dissipated energy ratio from decline to level can be used as the medium warning information of roadway water inrush.

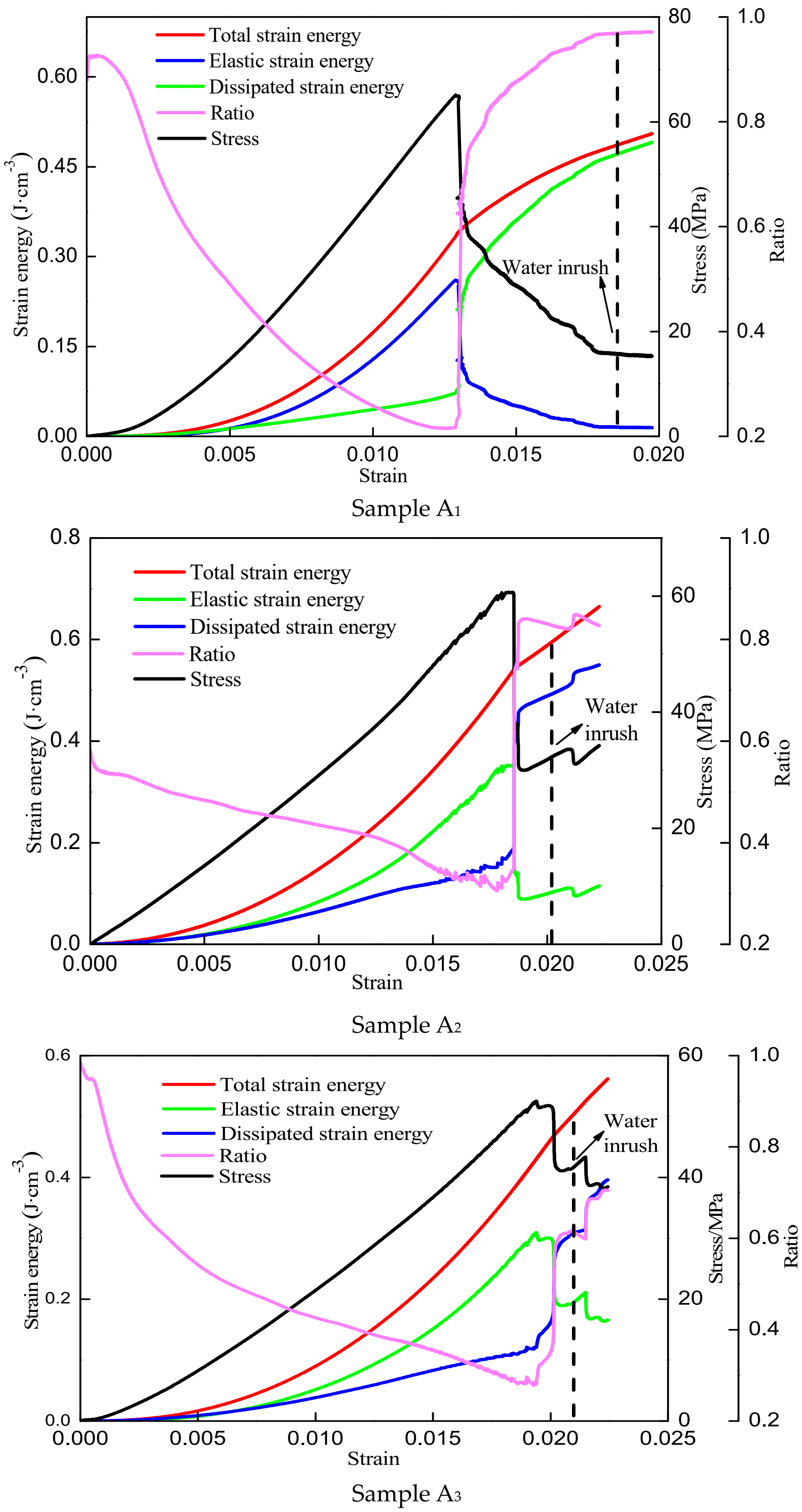

Figure 4. Evolution curves of strain energy during rock sample loading.

5.2. Infrared Radiation

Figure 5 shows the photo of the water inrush instant of the roadway in the laboratory. The water diversion channel is formed after the rock in the roadway reaches failure, and then water inrush occurs in the mine. Hence, the hole is selected as the analysis area of infrared radiation data, as shown in Figure 6. The evolution characteristics of *AIRT*, *IRCV*, *VSMIT*, and infrared thermal image in rock holes during the rock loading failure and water inrush were analyzed, and the precursors of roadway water inrush were identified.

Figure 5. Water inrush in roadway.

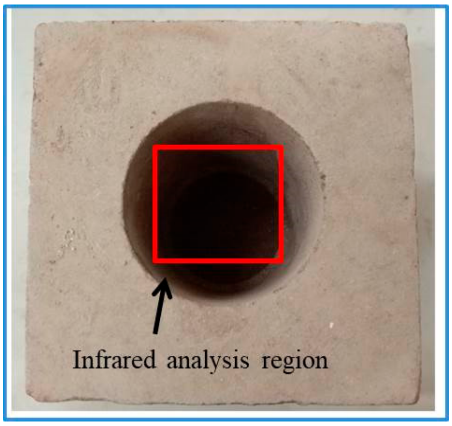

Figure 6. Infrared radiation analysis region.

5.2.1. AIRT

Figure 7 shows the time-varying curves of *AIRT*, *IRCV*, and *VSMIT* in the hole during the uniaxial rock sample loading. As shown in Figure 7, the *AIRT* in the hole of rock under loading showed a trend of stable fluctuation with the increase of stress during the process of rock uniaxial loading. The *AIRT* curves of rock samples A_1 and A_2 showed no obvious abnormal phenomena before rock failure, while the *AIRT* of the rock sample A_3 gradually increased, with a temperature rise of about 0.1 °C. However, the *AIRT* of rock samples A_1, A_2, and A_3 all dropped abruptly before water inrush, with a decrease temperature range of between 0.3~0.6 °C. This is due to the water seepage into the observation surface of the roadway absorbing part of the heat from the rock, resulting in a downward trend of *AIRT*. Therefore, the sudden drop of *AIRT* can be regarded as the precursor of water inrush. Two conditions must be satisfied to take a characteristic of infrared radiation index as a precursor: one is that all infrared radiation indexes of rock samples have this characteristic; the other is that this characteristic is easy to distinguish. The lead time of water inrush precursor of rock *AIRT* is 15~30 s before water inrush, hence *AIRT* decreased slightly and then increased.

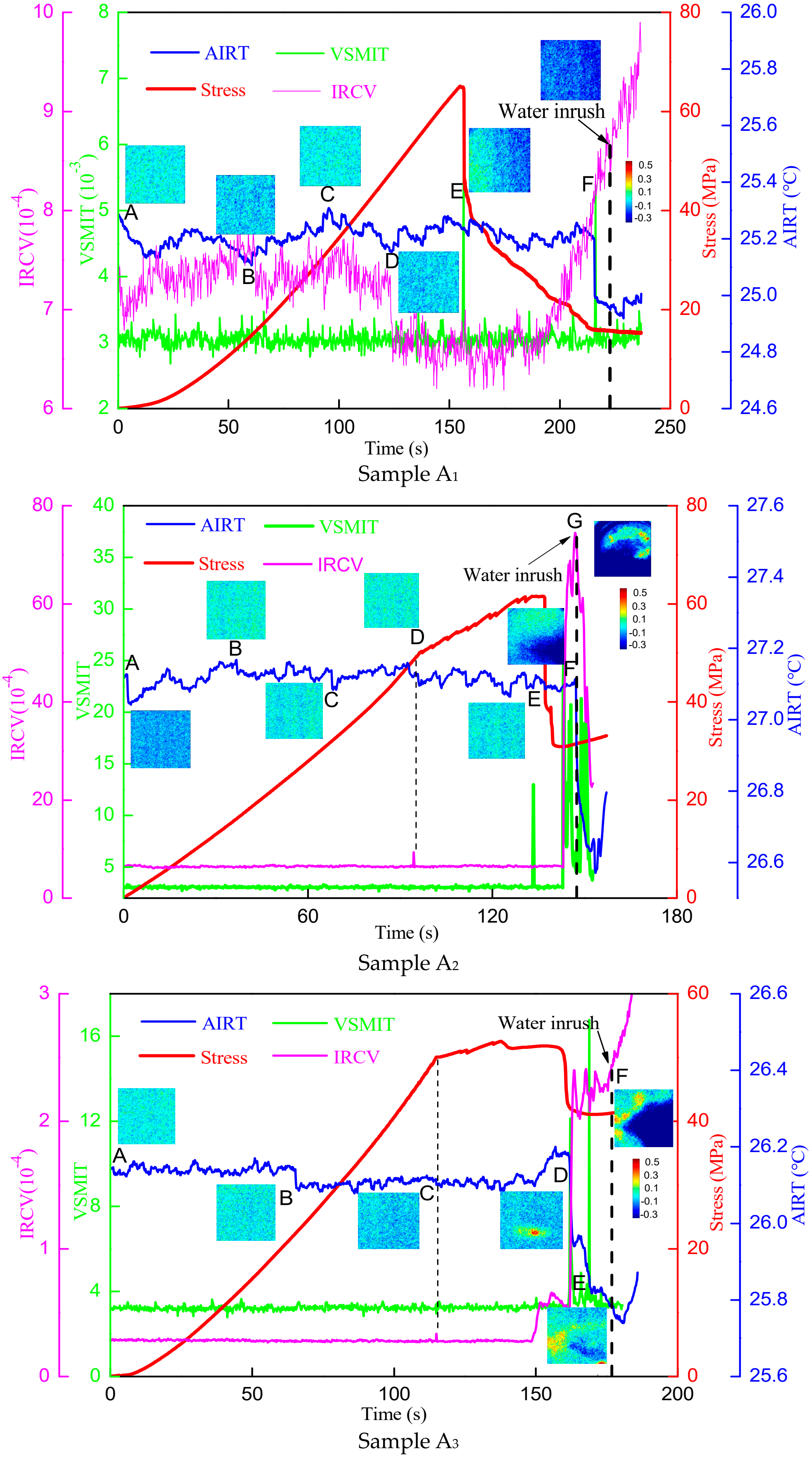

Figure 7. Evolution curves of *AIRT*, *IRCV*, and *VSMIT* during rock sample loading. A–G: different stages.

5.2.2. IRCV

The *IRCV* curve of rock sample A_1 shows a trend of steady fluctuation–decline–rise in the process of water inrush experiment under uniaxial loading, and the curve of *IRCV* mutates when loaded to 123 s, while the *IRCV* curves of rock samples A_2 and A_3 show a nearly horizontal trend, and both of them have a mutation in the middle of loading, with the occurrence moments of 94 s and 115 s, respectively. As shown in Figure 7, the *AIRT* value corresponding to the mutation of *IRCV* in the middle and late stages of loading decreases gradually, so the mutation of *IRCV* is caused by the mutation of infrared radiation standard deviation (σ). The authors propose that this is due to the rock having just entered the stage of unstable crack development, and microfracture events increase. The rock failure is dominated by microcracks induced by tensile failure. The tensile failure area corresponds to a drop in the rock surface temperature, while the shear failure area corresponds to a rise in the rock surface temperature, resulting in a gradual drop in *AIRT*. The increase of microfracture events leads to the occurrence of heating and cooling zones in different regions of the rock surface, and thus the standard deviation of corresponding infrared radiation temperature is suddenly changed. In conclusion, the curve of *IRCV* has suddenly changed in the middle and late stages of rock loading. Therefore, the *IRCV* mutation in the middle and late stages of rock loading can be regarded as the early precursor of water inrush.

As shown in Figure 7, when the *AIRT* of the rock drops suddenly before the water inrush (the precursor of water inrush), the *IRCV* curve of the rock increases or mutates gradually. Specifically, the *IRCV* curve of the rock sample A_1 increases gradually, and the rock samples A_2 and A_3 have a mutation. This feature, therefore, is not suitable as a precursor of roadway water inrush. If the water flows homogeneously into the roadway before water inrush, and the water has an amplification effect on the infrared radiation of rock [34], *AIRT* will drop abruptly, and the dispersion degree of infrared radiation temperature (σ) may also correspond to a sudden drop, which may cause no mutation in *IRCV*. If the water flows into the roadway inhomogeneously before water inrush, the *AIRT* will drop sharply and the differentiation of infrared radiation temperature (σ) will increase sharply, which will cause *IRCV* mutation. To sum up, *IRCV* curve mutation before water inrush is not universal, so it is not suitable as a precursor of roadway water inrush.

5.2.3. VSMIT

The *VSMIT* curve of all the rock samples shows a general horizontal trend during the roadway water inrush test, and the *VSMIT* increases abruptly when the rock failure, with the mutation range, is 0.01~0.03. Due to the universality, synchronism, and significance of *VSMIT* mutation characteristics at the rock failure [26], the first mutation of *VSMIT* can be regarded as a midterm precursor of water inrush. With the process of rock loading, the stress gradually drops to the residual stress. When the *AIRT* of the rock declines abruptly (the precursor of water inrush), the *VSMIT* of all rock samples mutate for the second time, with an increased range of 0.02~0.05. This is due to the water seepage increasing the dispersion degree of infrared radiation temperature of the two adjacent frames, which also indicates that the sudden drop in *AIRT* will be accompanied by the sudden increase of the *VSMIT* index. Therefore, the second mutation of *VSMIT* can be used as a precursor of water inrush.

5.2.4. Infrared Thermal Image

The above infrared radiation characteristics during the process of rock failure and water inrush were all obtained from the quantitative index analysis of infrared radiation, so only the time information of infrared radiation characteristics can be obtained. If the spatial information of infrared radiation during the process of rock failure and water inrush is needed, the infrared thermal image can be analyzed. To highlight the change of infrared radiation caused by the loading of the sample, and reduce the impact of the local radiation rate difference and environmental interference of the sample when processing the infrared radiation experimental data, the thermal image obtained during the loading process is processed as a difference [31], that is, the first thermal image at the beginning of the loading is subtracted from each thermal image, and the change of radiation temperature field is analyzed by using the image after the difference.

As shown in Figure 7, the infrared thermal image of rock sample A_1 before failure shows the changing trend of bright (A)–dark (B)–bright (C)–dark (D), corresponding to the decline (AB)–rise (BC)–decline (CD) of the AIRT curve, and the temperature difference between the left and right sides of the sample is obvious at the rock failure (the temperature on the left side is high while that on the right side is low), and the infrared thermal image at the precursory point (F) of the roadway water inrush becomes dark as a whole. At the beginning of the loading stage (AB) of sample A_2, the infrared thermal image of the rock sample changes from dark to bright, and there is no obvious abnormal change from point B to rock failure (E). The lower part of the rock shows the abnormal low-temperature area near the roadway water inrush precursory point (F), while the upper part of the infrared thermogram shows the abnormal high-temperature area when the roadway water inrush occurs, and the rest is the low-temperature area. At the beginning of loading stage (AB) of rock sample A_3, there is no obvious change in the infrared thermogram, and the infrared thermogram becomes dark at the BC stage, while the abnormal high-temperature area appears at the lower part of the rock sample (D). With the increase of stress, the abnormal high-temperature area becomes an abnormal low-temperature area in the roadway water inrush precursor (E), and the high-temperature area appears on the left side. The high-temperature area extends upward with the loading process, and part of the original high-temperature area is eroded by water, so the right side of the rock sample presents a large area of low temperature.

6. Multiparameter Normalization

6.1. Define

If the value range of the sample data is [Min, Max], then the normalized expression of linear function is

$$y = (x - \mathrm{Min})/(\mathrm{Max} - \mathrm{Min}) \tag{10}$$

where x and y are the values before and after conversion, respectively; Max and Min are the maximum and minimum values of samples, respectively.

The linear function normalization has the following properties: (1) the sample size relation remains unchanged; (2) the relative distance of samples remains unchanged. The variation trend of each physical quantity obtained by linear function normalization is consistent with the original data curve, which can well reflect the key information such as fluctuation and mutation points in the original data curve [44].

6.2. Analysis of Normalized Results

Based on the analysis of strain energy and infrared radiation characteristics of roadway water inrush, it is found that dissipative energy ratio, *AIRT*, *VSMIT*, and *IRCV* are suitable as the main parameters to predict roadway water inrush. In the practical application of multiparameter joint monitoring of a roadway water inrush disaster, due to the differences in the range and dimension of each parameter, and the different physical parameters in different coordinate systems, it is not conducive to the rapid and intuitive identification of the sequence of the occurrence of the abrupt point of each physical parameter, and this also affects the analysis of the correlation between each physical parameter. Therefore, it is necessary to normalize each parameter in order to comprehensively compare and analyze the variation rule of each parameter in the same scale, which can provide a comprehensive basis for the early warning of roadway water inrush disasters.

Figure 8 shows the normalized curves of stress, dissipated energy ratio, *AIRT*, *VSMIT*, and *IRCV* with time collected in a laboratory experiment of sandstone roadway water inrush. Based on the comprehensive analysis of all rock samples, it can be found that *IRCV* mutation occurs at the stage of 0.55~0.65 TWI (TWI is the time of water inrush) in the middle loading stage, which is the early precursor of water inrush in a sandstone roadway (as shown the EPWI in Figure 8). The dissipated energy ratio curve drops to the lowest point with the increase of stress, which is the first middle precursor of roadway water inrush (as shown by the FMPWI in Figure 8), and the early precursor is 20~33 s earlier than the middle precursor one. As the loading continues, rock sample failure occurs and accompanies the mutation of *VSMIT*, which is the second middle precursor of roadway water inrush (as shown by SMPWI in Figure 8). Thereafter, the stress drops rapidly and *AIRT* decreases abruptly at about 0.95~0.98 TWI after it decreases to residual strength. This is the first precursor of roadway imminent water inrush (as shown by FPIWI in Figure 8), corresponding to the sudden increase of *VSMIT*, which is the second precursor of imminent water inrush (as shown by SPIWI in Figure 8), indicating that roadway water inrush may occur at any time.

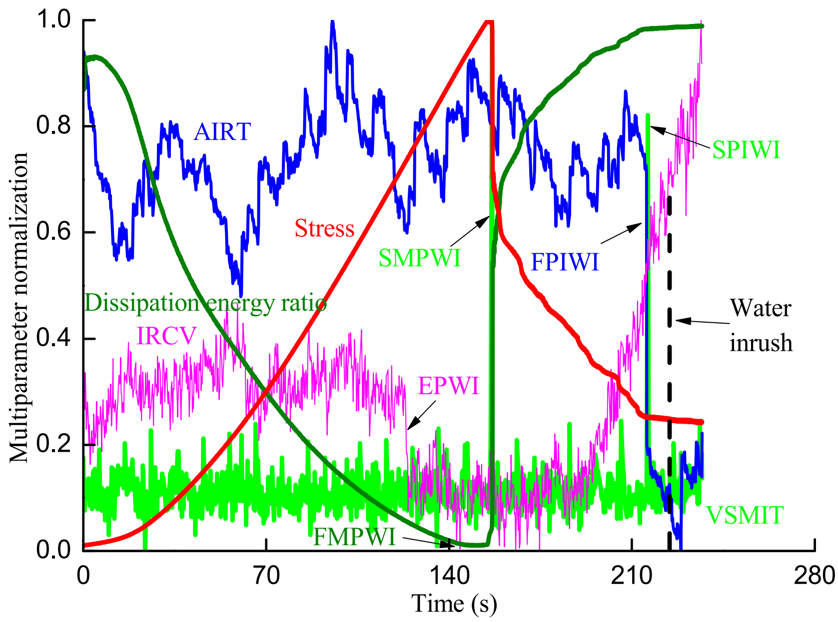

Sample A1

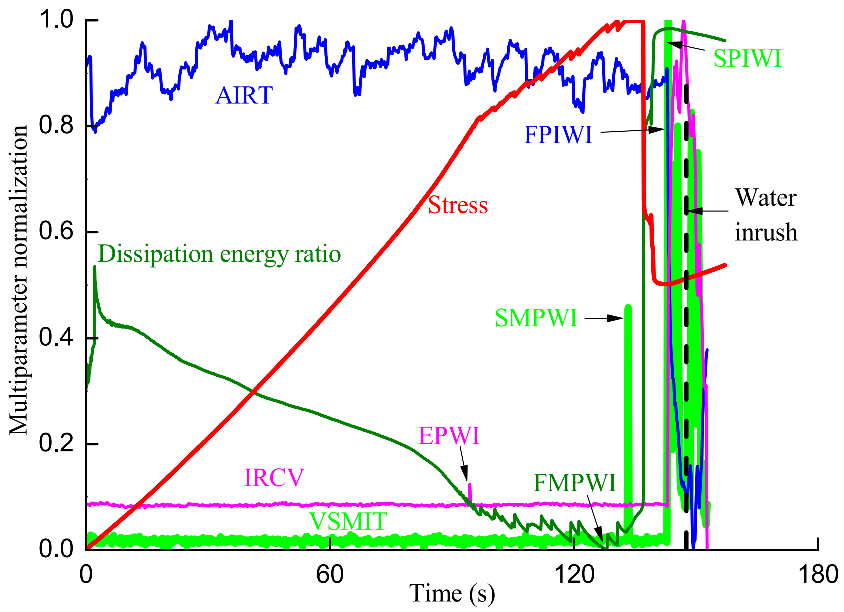

Sample A2

Figure 8. *Cont.*

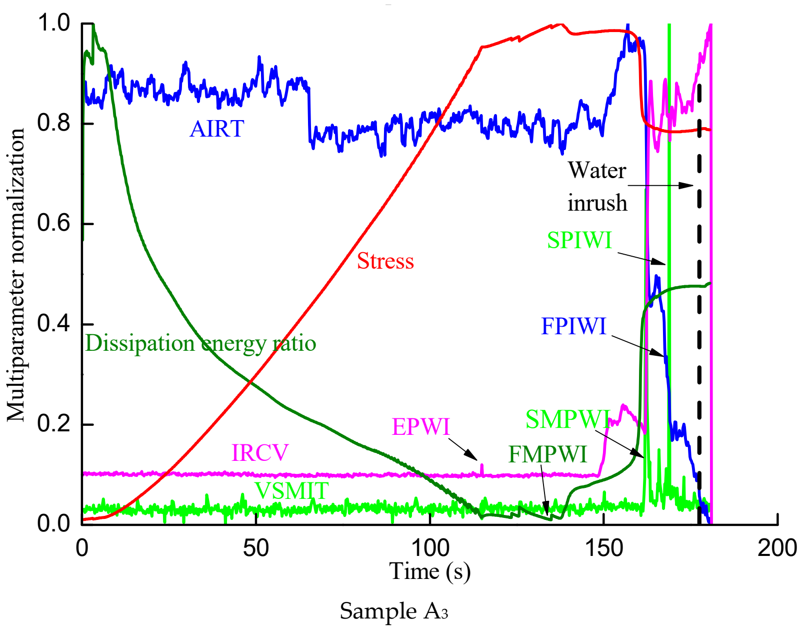

Figure 8. Multiparameter normalization curve in the process of roadway water inrush.

7. Discussion

(1) Due to the nonlinear process of roadway water inrush, the complexity and diversity of influencing factors, and the control of the accuracy of monitoring technology, the prediction of roadway water inrush with a single parameter has great limitations. The precursor of roadway water inrush cannot be accurately and effectively identified in practical application, which may lead to the problem of false alarms or missed alarms. The precursors of roadway water inrush can be identified more quickly by the normalized treatment of each physical parameter in the process of roadway water inrush. At the same time, the correlation between precursor information of roadway water inrush was obtained. Comprehensively considering and analyzing the precursors' information for roadway water inrush and its correlation, the hierarchical warning of a roadway water inrush disaster can be obtained and the accuracy and reliability of roadway water inrush warning can be improved.

(2) *AIRT* reflects the whole infrared radiation intensity of the rock surface, but there may be different heating and cooling zones in the process of rock loading and fracture due to which the *AIRT* remains unchanged. The *IRCV* of rocks reflects the dispersion degree of the original infrared radiation temperature, which has the advantage of avoiding the unit of measurement of data and neglecting the influence of numerical magnitude. Compared with *AIRT* index, *IRCV* can reflect the dispersion characteristics of infrared radiation caused by temperature rise and temperature drop areas. *VSMIT* reflects the dispersion degree of the difference in infrared radiation temperature between two adjacent frames. Compared with *IRCV* index, it eliminates the cumulative heating effect of loaded rock, and is easier to monitor the process of rock failure, instability, and seepage. From the sensitivity of *IRCV* index to the unstable crack development stage of rock, *IRCV* mutation was proposed as the early precursor of roadway water inrush. Based on the feature that *VSIMT* can monitor rock failure, the first mutation of *VSMIT* was proposed as the medium-term precursor of roadway water inrush. Established from the characteristic that *AIRT* and *VSMIT* are sensitive to water, the sudden drop of *AIRT* and the second mutation of *VSMIT* were proposed as the precursor of roadway imminent water inrush. In this paper, combined with the advantages of *AIRT*, *IRCV*, and *VSMIT*, the multiparameters precursory characteristics of roadway water inrush were determined.

(3) Infrared observation technology is a promising new method for monitoring rock samples, which has the advantages of noncontact and strong anti-interference, and can

be used for monitoring and warning the stability of bearing rock and surrounding rock of tunnels in underground engineering. Acoustic emission monitoring technology can detect the time and location of a microfracture in a rock mass. Therefore, acoustic emission monitoring (internal) and infrared radiation monitoring (external) should be combined in subsequent roadway water inrush experiments and underground engineering construction sites. Acoustic emission (AE) will be used to locate the water-conducting fissure passage in the rock, and the change rules and coupling effects of the stress field, infrared radiation temperature field, and seepage field before water inrush in underground engineering will be studied in order to build a multifield coupling model of "stress–temperature–seepage" of roadways based on infrared radiation and reveal the mechanism of water inrush in underground engineering.

8. Conclusions

The forecast of highway water inrush with a single parameter has significant limits because of the nonlinear nature of the roadway water inrush process, the complexity and variety of contributing elements, and the control of the accuracy of monitoring equipment. The issue of false alerts or missed alarms may arise from the inability to precisely and efficiently identify the antecedent of highway water inrush in practical application. The normalized treatment of each physical parameter in the process of highway water inrush may help identify the antecedents of roadway water inrush more promptly. The association between the precursor data of the highway water inrush was discovered concurrently. The following conclusions were drawn:

(1) Dissipative energy ratio, AIRT, VSMIT, and IRCV are suitable as precursor indexes for roadway water inrush prediction, and can be used to monitor and predict the occurrence of roadway water inrush.
(2) The midterm mutation of IRCV can be used as the early precursor information of roadway water inrush. The turning point of dissipation energy ratio from decreasing to level and the sudden change of VSMIT during rock failure can be used as the medium term precursor information of roadway water inrush. AIRT and VSMIT mutation after rock failure can be used as precursor information of roadway imminent water inrush.
(3) By using the normalization of linear function transformation to normalize the multi-physical parameters in the process of roadway water inrush monitoring, this realizes early warning for roadway water inrush as "early precursor–medium precursor–final precursor". In future research, we will select representative mining sections in coal and rock mining damage areas, conduct infrared radiation observations at different mining stages (damage states), compare and analyze onsite monitoring and laboratory test results, and establish a graded precursor warning based on onsite infrared radiation data.

Author Contributions: K.C.: conceptualization, writing—original draft, and experiments; F.D.: conceptualization, supervision, and project administration; L.M.: supervision and project administration; N.M.K.: software and data curation, writing—original draft; methodology; T.F.: visualization; S.S.A.: investigation and data curation; S.H.: Formal analysis; M.A.: experiments. All authors have read and agreed to the published version of the manuscript.

Funding: This research was supported by Anhui Provincial Scientific Research Preparation Plan Project (2022AH050596). The authors also acknowledge the Researchers Supporting Project number (RSP2023R496), King Saud University, Riyadh, Saudi Arabia.

Institutional Review Board Statement: Not applicable.

Data Availability Statement: The data that support the findings of this study are available from the corresponding author upon reasonable request.

Conflicts of Interest: The authors declare no conflict of interest.

References

1. Ma, D.; Duan, H.; Zhang, J.; Bai, H. A state-of-the-art review on rock seepage mechanism of water inrush disaster in coal mines. *Int. J. Coal Sci. Technol.* **2022**, *9*, 50. [CrossRef]
2. Chi, X.; Yang, K.; Wei, Z. Breaking and mining-induced stress evolution of overlying strata in the working face of a steeply dipping coal seam. *Int. J. Coal Sci. Technol.* **2021**, *8*, 614–625. [CrossRef]
3. Guo, P.; Gu, J.; Su, Y.; Wang, J.; Ding, Z. Effect of cyclic wetting–drying on tensile mechanical behavior and microstructure of clay-bearing sandstone. *Int. J. Coal Sci. Technol.* **2021**, *8*, 956–968. [CrossRef]
4. Liu, Z.; Wang, G.; Li, J.; Li, H.; Zhao, H.; Shi, H.; Lan, J. Water-immersion softening mechanism of coal rock mass based on split Hopkinson pressure bar experiment. *Int. J. Coal Sci. Technol.* **2022**, *9*, 61. [CrossRef]
5. Liu, A.; Liu, S.; Liu, P.; Wang, K. Water sorption on coal: Effects of oxygen-containing function groups and pore structure. *Int. J. Coal Sci. Technol.* **2021**, *8*, 983–1002. [CrossRef]
6. Lou, J.; Gao, F.; Yang, J.; Ren, Y.; Li, J.; Wang, X.; Yang, L. Characteristics of evolution of mining-induced stress field in the longwall panel: Insights from physical modeling. *Int. J. Coal Sci. Technol.* **2021**, *8*, 938–955. [CrossRef]
7. Hou, L.; Cao, K.; Muhammad Khan, N.; Jahed Armaghani, D.; Alarifi, S.S.; Hussain, S.; Ali, M. Precursory Analysis of Water-Bearing Rock Fracture Based on The Proportion of Dissipated Energy. *Sustainabilty* **2023**, *15*, 1769. [CrossRef]
8. Vervoort, A. Various phases in surface movements linked to deep coal longwall mining: From start-up till the period after closure. *Int. J. Coal Sci. Technol.* **2021**, *8*, 412–426. [CrossRef]
9. Wang, J.; Yang, S.; Wei, W.; Zhang, J.; Song, Z. Drawing mechanisms for top coal in longwall top coal caving (LTCC): A review of two decades of literature. *Int. J. Coal Sci. Technol.* **2021**, *8*, 1171–1196. [CrossRef]
10. Ma, J.J.; Guan, J.W.; Duan, J.F.; Huang, L.C.; Liang, Y. Stability analysis on tunnels with karst caves using the distinct lattice spring model. *Undergr. Space.* **2021**, *6*, 469–481. [CrossRef]
11. Huang, L.C.; Ma, J.J.; Lei, M.F.; Liu, L.H.; Lin, Y.X.; Zhang, Z.Y. Soil-water inrush induced shield tunnel lining damage and its stabilization: A case study. *Tunn. Undergr. Space Technol.* **2020**, *97*, 103290. [CrossRef]
12. Ma, J.J.; Chen, J.J.; Chen, W.X.; Huang, L.C. A coupled thermal-elastic-plastic-damage model for concrete subjected to dynamic loading. *Int. J. Plasticity.* **2022**, *153*, 103279. [CrossRef]
13. Ma, J.J.; Chen, J.J.; Guan, J.W.; Lin, Y.X.; Chen, W.X.; Huang, L.C. Implementation of Johnson-Holmquist-Beissel model in four-dimensional lattice spring model and its application in projectile penetration. *Int. J. Impact Eng.* **2022**, *170*, 104340. [CrossRef]
14. Cao, K.; Ma, L.; Wu, Y.; Khan, N.; Yang, J. Using the characteristics of infrared radiation during the process of strain energy evolution in saturated rock as a precursor for violent failure. *Infrared Phys. Technol.* **2020**, *109*, 103406. [CrossRef]
15. Yang, D.; Ning, Z.; Li, Y.; Lv, Z.; Qiao, Y. In situ stress measurement and analysis of the stress accumulation levels in coal mines in the northern Ordos Basin, China. *Int. J. Coal Sci. Technol.* **2021**, *8*, 1316–1335. [CrossRef]
16. Feng, F.; Chen, S.; Zhao, X.; Li, D.; Wang, X.; Cui, J. Effects of external dynamic disturbances and structural plane on rock fracturing around deep underground cavern. *Int. J. Coal Sci. Technol.* **2022**, *9*, 15. [CrossRef]
17. He, S.; Qin, M.; Qiu, L.; Song, D.; Zhang, X. Early warning of coal dynamic disaster by precursor of AE and EMR "quiet period". *Int. J. Coal Sci. Technol.* **2022**, *9*, 46. [CrossRef]
18. Zhang, L.; Kan, Z.; Zhang, C.; Tang, J. Experimental study of coal flow characteristics under mining disturbance in China. *Int. J. Coal Sci. Technol.* **2022**, *9*, 66. [CrossRef]
19. Ali, M.; Wang, E.; Li, Z.; Wang, X.; Khan, N.M.; Zang, Z.; Alarifi, S.S.; Fissha, Y. Analytical Damage Model for Predicting Coal Failure Stresses by Utilizing Acoustic Emission. *Sustainabilty* **2023**, *15*, 1236. [CrossRef]
20. Cui, R.; Cao, K.; Li, X.; Khan, R.M.A.; Khan, N.M.; Liu, W.; Gao, Q.; Wang, F. The Infrared Radiation Characteristics of Sandstone Fracture Seepage under Coupled Stress-Hydro Effect. *Sustainabilty* **2022**, *14*, 16454. [CrossRef]
21. Liu, S.; Wu, L.; Wu, Y. Infrared radiation of rock at failure. *Int. J. Rock Mech. Min.* **2006**, *43*, 972–979. [CrossRef]
22. Zhao, Y.; Jiang, Y.J. Acoustic emission and thermal infrared precursors associated with bump-prone coal failure. *Int. J. Coal Geol.* **2010**, *83*, 11–20. [CrossRef]
23. Cao, K.W.; Dong, F.R.; Liu, W.; Naseer, M.K.; Cui, R.Y.; Li, X.C.; Hussain, S.; Saad, S.A.; Niu, D.D. Infrared radiation denoising model of "sub-region-Gaussian kernel function" in the process of sandstone loading and fracture. *Infrared Phys. Technol.* **2023**, *129*, 104583. [CrossRef]
24. Wang, C.; Lu, Z.; Liu, L.; Chuai, X. Predicting points of the infrared precursor for limestone failure under uniaxial compression. *Int. J. Rock Mech. Min. Sci.* **2016**, *88*, 34–43. [CrossRef]
25. Mineo, S.; Pappalardo, G. The use of infrared thermography for porosity assessment of intact rock. *Rock Mech. Rock Eng.* **2016**, *49*, 3027–3039. [CrossRef]
26. Pappalardo, G.; Mineo, S.; Zampelli, S.P.; Cubito, A. Infrared Thermography proposed for the estimation of the Cooling Rate Index in the remote survey of rock masses. *Int. J. Rock Mech. Min. Sci.* **2016**, *83*, 182–196. [CrossRef]
27. Ma, L.; Sun, H.; Zhang, Y.; Zhou, T.; Li, K.; Guo, J. Characteristics of infrared radiation of coal specimens under uniaxial loading. *Infrared Phys. Technol.* **2016**, *49*, 1567–1572. [CrossRef]
28. Sun, X.; Xu, H.; He, M.; Zhang, F. Experimental investigation of the occurrence of rockburst in a rock specimen through infrared thermography and acoustic emission. *Int. J. Rock Mech. Min. Sci.* **2017**, *93*, 250–259. [CrossRef]
29. Sun, H.; Ma, L.; Adeleke, N.; Zhang, Y. Background thermal noise correction methodology for average infrared radiation temperature of coal under uniaxial loading. *Infrared Phys. Technol.* **2017**, *81*, 157–165. [CrossRef]

30. Asakura, T.; Kojima, Y.J.T.; Technology, U.S. Tunnel maintenance in Japan. *Tunn. Undergr. Space Technol.* **2003**, *18*, 161–169. [CrossRef]
31. Liu, S.; Zhang, Y.; Wu, L. Infrared radiation characteristics of concrete rupture and water seepage process. *Chin. J. Rock Mech. Eng.* **2009**, *28*, 53–58.
32. Dou, H.T.; Xue, Y.D. Experimental study on influencing factors of infrared radiation characteristics of tunnel lining leakage. *Chin. J. Rock Mech. Eng.* **2011**, *30*, 9.
33. Zhang, Y.B.; Liang, P.; Liu, X.X.; Tian, B.Z. Study on infrared spatiotemporal evolution characteristics of water inrush in soft roadway. *Coal Sci. Technol.* **2015**, *44*, 6.
34. Wu, L.; Wang, J. Infrared radiation features of coal and rocks under loading. *Int. J. Rock Mech. Min. Sci. Geomech. Abstr.* **1998**, *35*, 332419. [CrossRef]
35. Liu, S.J.; Zhang, Y.B.; Chen, Q.L. The variation characteristics of infrared radiation in the process of wet-rock stress. *J. Northeast Univ.* **2010**, *1*, 4.
36. Ma, L.; Sun, H.; Zhang, Y.; Hu, H.; Zhang, C.J.S. The role of stress in controlling infrared radiation during coal and rock failures. *Strain* **2018**, *54*, e12295. [CrossRef]
37. Liu, S.J.; Huang, J.W.; Wu, L.X.; Zhang, Y.B.; Tian, B.Z. Quantitative analysis methods of infrared radiation temperature field variation in rock loading process. *Chin. J. Rock Mech. Eng.* **2015**, *34*, 9.
38. Ma, L.; Zhang, Y. An Experimental Study on Infrared Radiation Characteristics of Sandstone Samples Under Uniaxial Loading. *Rock Mech. Rock Eng.* **2019**, *52*, 3493–3500. [CrossRef]
39. Yang, S.Q.; Dong, Y.; Wang, G.Y.; Chen, D.C.; Zhang, J.Y. Study on the evolution law of surface infrared radiation during shale deformation. *Chin. J. Undergr. Space Eng.* **2019**, *15*, 7.
40. Liu, S.J.; Wu, L.X. Comparison of infrared radiation characteristics between brittle rock and plexiglass under stress. *Chin. J Rock Mech. Eng.* **2007**, *26*, 4183–4188.
41. Liu, W.; Yang, K.; Zhang, S.; Zhang, Z.N.; Xu, R.J. Energy evolution and water immersion-induced weakening in sandstone roof of coal mines. *Int. J. Coal Sci. Technol.* **2022**, *9*, 53. [CrossRef]
42. Du, F.; Ma, J.; Guo, X.; Wang, T.F.; Dong, X.H.; Li, J.S.; He, S.L.; Nuerjuma, D. Rockburst mechanism and the law of energy accumulation and release in mining roadway: A case study. *Int. J. Coal Sci. Technol.* **2022**, *9*, 67. [CrossRef]
43. Ma, L.; Sun, H.J.I.P. Spatial-temporal infrared radiation precursors of coal failure under uniaxial compressive loading. *Infrared Phys. Technol.* **2018**, *93*, 144–153. [CrossRef]
44. Cao, K.W.; Xu, Y.J.; Naseer, M.K.; Li, X.C.; Cui, R.Y.; Hussain, S.; Danial, J.A.; Alarifi, S.S. A comprehensive model for evaluating infrared radiation and acoustic emission characteristics of sandstone fracture. *Eng. Fract. Mech.* **2023**, *283*, 109217. [CrossRef]